PUBLISHED VERSION

Binder, Benjamin James; Landman, Kerry A.; Simpson, Matthew J.; Mariani, Michael; Newgreen, Donald Francis

http://link.aps.org/doi/10.1103/PhysRevE.78.031912

http://hdl.handle.net/2440/68178

Modeling proliferative tissue growth: A general approach and an avian case study

Benjamin J. Binder, Kerry A. Landman,* and Matthew J. Simpson
Department of Mathematics and Statistics, The University of Melbourne, Melbourne, Victoria 3010, Australia

Michael Mariani and Donald F. Newgreen
Department of Embryology, Murdoch Childrens Research Institute, Parkville, Victoria 3052, Australia

During development, tissues often undergo rapid physical expansion due to cell proliferation. Continuous and discrete models of one- and two-dimensional tissue growth are developed and applied to observational data of the developing avian gut, where the gut tissue cells undergo dramatic proliferation. The discrete cellular automata model provides results at the level of individual cells that reflect a realistic stochasticity and nonuniformity expected in cellular systems. Averaging the discrete results predicts population-level properties of the system, which match those of the continuous model. This dual approach provides an understanding of the interaction between the individual-level and population-level aspects of a developmental growth process. Both models are applied to a case study involving the developing intestinal tract of a quail embryo. A nonuniform growth model accurately predicts the positions of measurable biological landmarks within the growing tissue. Furthermore, the discrete model provides a framework for modeling the interactions between growing tissues and other biological mechanisms, such as cell motility and proliferation on an expanding tissue.

PACS number(s): 87.17.$-$d, 87.18.$-$h, 87.85.$-$d

I. INTRODUCTION

Embryogenesis is associated with dramatic morphogenesis. Many of these shape-changing processes are very rapid and are achieved primarily by reorganization of cells in space. An example of this is convergent extension [1–4], whereby cell intercalation transforms a short broad tissue to a narrower longer structure. In many embryos, particularly anamniotes, this occurs with minimal increase in the volume of the tissue whose shape is changing. Amniote embryos also undergo cell reorganization over a short time scale during the initial phase of morphogenesis. But, having access to an extraembryonic nutrient supply, this is followed, over a long time scale, by large-scale growth involving cell proliferation and dramatic expansion of tissue volume.

We are interested in modeling the development of the enteric nervous system (ENS) in the intestine of amniote vertebrates, such as birds, rodents, and humans. During the earliest and rapid stages of intestinal morphogenesis, the gut sculpts itself to form a tube from wide bilateral flat layers [5]. After this early stage, ENS development involves a population of motile and highly proliferative neural crest (NC) cells invading the gut tissues as a unidirectional wave [6–8]. During the relatively long time period for NC colonization, the gut in amniotes undergoes extensive growth in cell number by proliferation, resulting in massive elongation, as illustrated in Fig. 1. Restriction of gut cell proliferation results in a short gut tube [9]. Here we consider this later phase of growth of the overall gut tube.

Tissue growth may interact with other developmental processes. For example, growth may alter the spatial distribution of cells or morphogens within the developing tissue, thereby mediating cellular and molecular interactions. This occurs during ENS development. In these cases, it can be important to understand how the tissue growth is coupled to other developmental processes.

Mathematical models have been developed to investigate various aspects of embryogenesis and development, such as pattern formation [10,11] and limb bud development [12,13]. Theoretical mathematical models that couple tissue growth with other processes have been studied, for example, spatiotemporal pattern formation within expanding domains [14–19], cell invasion on a growing domain [6,8], and tissue growth coupled to the movement of morphogens [20]. However, none of these previous investigations have used observational data to develop or parametrize the tissue growth model. To overcome this limitation, we develop a model for
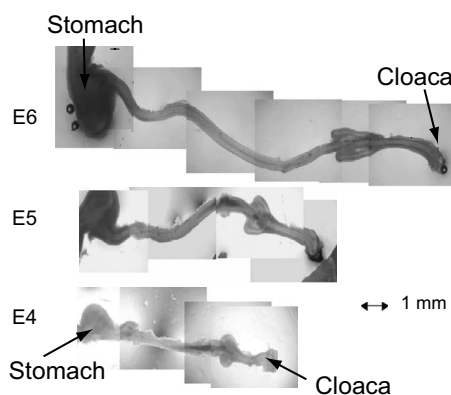
FIG. 1. Images of quail guts from embryonic age four days to six days (E4 to E6). The intestinal cell number in the region (small plus large intestine, excluding the stomach) increases from less than 850 000 at E4 to approximately 2 500 000 at E6 and continues to increase in number (approximately 4 000 000 at E7). This results in an increase in cell volume, whereby there is an increase in length without narrowing, accompanied by radial expansion in some regions.

*k.landman@ms.unimelb.edu.au

031912-1

tissue growth due to cell proliferation, parametrized by real biological growth measurements. Images of developing quail guts (Fig. 1) are used to describe and parametrize two types of tissue growth models, one continuous and the other discrete.

The continuous model is conceptually simple, easy to implement, and can be directly coupled to a continuum model to describe the motility of cells or morphogens within the growing tissue [6,8]. In parallel, a discrete stochastic cellular automata (CA) model of tissue growth is also developed. The CA model provides results at the level of an individual cell which reflect realistic stochasticity and nonuniformity. Analysis of the discrete mechanism connects the continuum and discrete models. This dual approach provides insight into the interaction between the individual-level and population-level aspects of a development process [21–23].

To motivate our analysis, we consider a growing population of cells, with no limitation for resources, which will form the developing tissue. If the number of cells P grows through mitotic division, then $dP/dt = \sigma P$, where σ is a constant. If the cell density ρ is uniform, the number of cells is related to the tissue geometry $P = \rho V$, where V is the volume of tissue. If the tissue has a regular volume with length X, width Y, and thickness Z then

$$V = XYZ, \quad \frac{dV}{dt} = \sigma V. \tag{1}$$

Clearly the volume grows exponentially with time, with $V(t) = V(0)e^{\sigma t}$. Expanding the temporal derivative in Eq. (1) gives

$$\frac{1}{X}\frac{dX}{dt} + \frac{1}{Y}\frac{dY}{dt} + \frac{1}{Z}\frac{dZ}{dt} = \sigma. \tag{2}$$

The three terms on the left of Eq. (2) represent (i) the time rate of change of length per unit length, (ii) the time rate of change of width per unit width and (iii) the time rate of change of thickness per unit thickness of the tissue. Assuming each of these components to be constant, denoted by σ_X, σ_Y, and σ_Z, respectively, the net growth rate σ can be written as the sum of these constant growth rates, namely,

$$\sigma = \sigma_X + \sigma_Y + \sigma_Z. \tag{3}$$

Combined with Eq. (2), this gives

$$X(t) = X(0)e^{\sigma_X t}, \quad Y(t) = Y(0)e^{\sigma_Y t}, \quad Z(t) = Z(0)e^{\sigma_Z t}. \tag{4}$$

Therefore, if the number of cells in a uniform density tissue grows exponentially with time, it is possible for the length, width, and thickness of the tissue to each grow exponentially with time. In particular, the volume may grow with a fixed growth rate σ. However, the relative growth rates of the three orthogonal dimensions of that volume can differ, since there are infinitely many choices of σ_X, σ_Y, and σ_Z that satisfy Eq. (3).

This idealization will be useful to characterize observational data where the dimensions of a growing tissue increase exponentially with time, as occurs during the development of the intestinal tract in a quail embryo. As discussed in Sec. IV,

the gut tissue undergoes large-scale elongation and some radial growth, with insignificant change in thickness (Fig. 1). The elongation and radial expansion can both be described by exponential growth. The growth rates for the case study can be interpreted in terms of an exponential increase in the total cell number.

II. TISSUE GROWTH MODELS

The growth of the developing three-dimensional gut tissues (Fig. 1) is idealized as a series of cylindrical shells positioned end to end, each with a particular cross-sectional area normal to the longitudinal axis. The thickening of the cross-sectional area is small compared to the elongation and radial expansion, so that the overall growth can be approximated by the increase in the area of the outer cylindrical surface. Each cylindrical shell is cut lengthwise, so becoming a flat rectangular plate with a fixed thickness [Z in Eq. (1)]. Therefore, we need only consider the growth of a rectangular region in the Cartesian plane.

Continuous and discrete models of two-dimensional rectangular tissue growth will be formulated and analyzed in detail. To motivate the ideas and methods, we first consider uniaxial growth, where growth is along one axis only. We compare the discrete and continuum models and discuss the statistical distribution arising from the discrete model. Then we consider biaxial growth, where growth is along both axes. In Sec. III these models are modified to represent nonuniform elongation. A case study of the development of avian gut tissues is given in Sec. IV, followed by discussion and conclusions.

A. Continuum uniform uniaxial growth model

Consider a single growing rectangular piece of tissue of length $0 < x < X(t)$ and width $0 < y < Y(t)$. For uniaxial growth in the x direction, the width remains constant, so we write $Y(t) = Y$. The elongation implies that there is a local velocity $u(x,t)$ such that a point x moves to the point $x + u(x,t)\Delta t$, during a small time interval Δt. By considering a small element Δx of the domain, it can be shown that [6,8,16,19]

$$\frac{dX}{dt} = \int_0^{X(t)} \frac{\partial u}{\partial x} dx. \tag{5}$$

For uniform growth the growth rate is independent of position [6], and can be written as

$$\frac{\partial u}{\partial x} = F(t), \quad 0 < x < X(t). \tag{6}$$

Combining Eqs. (5) and (6) gives

$$\frac{1}{X}\frac{dX}{dt} = F(t). \tag{7}$$

Equation (7) may be interpreted in two ways, namely, (i) if $F(t)$ is known, the growth of $X(t)$ is defined by Eq. (7), and alternatively (ii) if $X(t)$ is known, then Eq. (7) determines $F(t)$. Typically, $X(t)$ is known, since this quantity can be
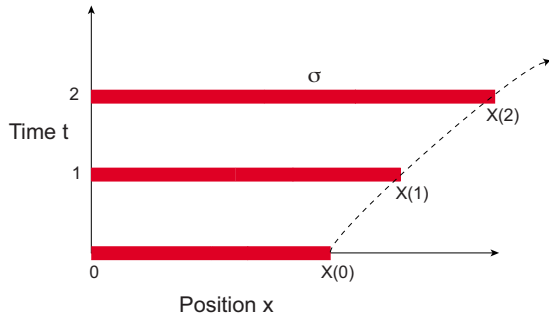
FIG. 2. (Color online) Schematic space-time diagram for uniaxial tissue elongation.

measured. Note that, without loss of generality, we have chosen $u(0,t)=0$.

If $F(t)$ is a constant, given by σ_X, then Eq. (7) implies

$$X(t) = X(0)e^{\sigma_X t}. \tag{8}$$

A schematic representation in a space-time diagram is given in Fig. 2. The time evolution of the position of the trajectory of a general point x_0, where $0 < x_0 < X(0)$, is given by

$$\frac{dx}{dt} = u(x,t), \quad x(0) = x_0. \tag{9}$$

The local growth rate determines the velocity field as

$$u(x,t) = \int_0^x \frac{\partial u}{\partial \xi} d\xi = \sigma_X x. \tag{10}$$

Hence the evolving path of such a point is

$$x(t) = x_0 e^{\sigma_X t}. \tag{11}$$

Equation (11) gives the continuum paths of any point within the tissue.

B. Cellular automata uniaxial growth model

Uniaxial elongation of a two-dimensional tissue will now be simulated with a discrete CA model. The model is developed on a rectangular lattice in the x-y plane. Since we are considering elongation only at this stage, the lattice width Y remains constant while the lattice length is variable. A single cell or group of neighboring cells in the tissue is idealized as a unit square agent on the lattice. This allows us to model the tissue elongation on a variety of scales. A discrete point within the lattice is represented with the coordinates (x,y), which denotes the top right-hand corner of a unit square agent. The origin is located in the lower left-hand corner of the lattice. An agent is represented by a circle whose center is positioned at the top right-hand corner of the square agent. The initial length of the lattice $X(0)$ is a positive integer.

The length of the lattice increases according to the proliferation mechanism illustrated in Fig. 3(a). If an agent at (x,y) proliferates, the original agent moves to $(x+1,y)$, and a new (yellow) agent is inserted at (x,y). All agents to the right of (x,y) move one unit in the positive x direction. There is no movement in the y direction; hence the rows in the lattice are independent. By considering several adjacent rows, this one-
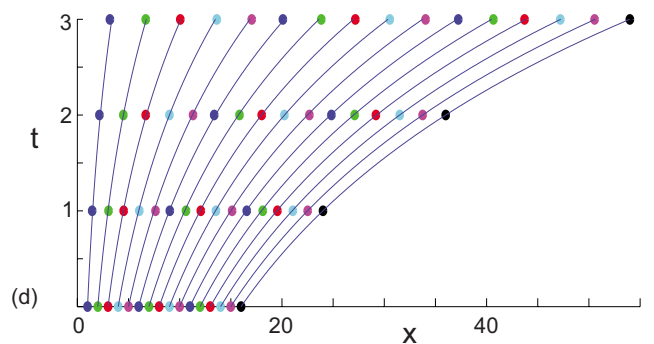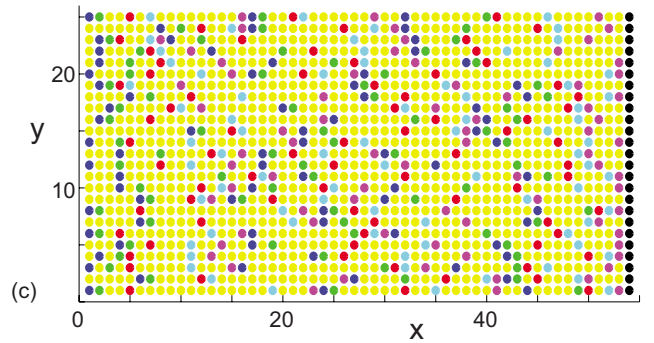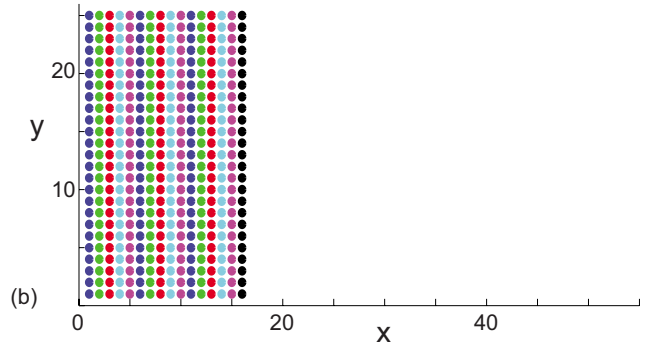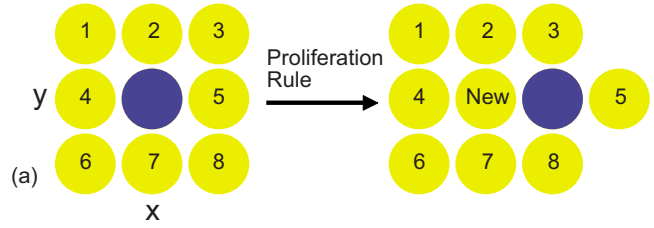

FIG. 3. (Color online) Cellular automata model and paths determined by the continuum model. (a) CA proliferation mechanism. In (b)-(d) the values of the parameters for the initial length and the growth rate are $X(0)=16$ and $\sigma_X=0.41$. (b) Columns of agents with the same color at $t=0$ will be tracked for $t>0$, $Y=25$. The black column is the end of the tissue. (c) Positions of tracked agents at $t=3$. (d) Space-time diagram of the paths (solid curves) from the continuum model and the average values (markers) $\bar{p}(x_0,t)$ from $N=10$ simulations of the CA model.

dimensional mechanism can be used to represent the uniaxial elongation of a two-dimensional tissue with constant width [Fig. 3(b)].

Consider an agent initially at position (x_0,y_0). Here, x_0 and y_0 are positive integers, such that $1 \leq x_0 \leq X(0)$ and $1 \leq y_0 \leq Y$. We are interested in tracking the position of this

agent at later times. To this end, for the jth realization of a simulation, we define $p_j(x_0,y_0,t)$ as its horizontal position. By definition, at $t=0$, each colored column in Fig. 3(b) has $p_j(x_0,y_0,0)=x_0$, for all rows y_0. Figure 3(a) shows the effect of the proliferation rule on the position of an (blue) agent being tracked.

The length of the lattice is increased at the same rate as the continuum model. Equation (8) shows that the increase in the length $X(t)$ from time t to $t+1$ in the continuum model is $X(t)(e^{\sigma_X}-1)$. For a single time step of the CA algorithm, n agents in each row are chosen to proliferate at randomly selected positions. Here, n is the nearest integer value or "round" of $p_j(X(0),y_0,t)(e^{\sigma_X}-1)$. The n new agents are inserted to the left of the chosen agents, as described in Fig. 3(a). When a new agent is inserted, the position of $p_j(X(0),y_0,t)$ is updated before the next insertion.

Figure 3(c) illustrates a single simulation with the initial condition given in Fig. 3(b). The position of the black column at $t=3$ in Fig. 3(c) is $p_j(16,y_0,3)=54$, which is the same as the continuum result. Other choices of $X(0)$, σ_X, and t may give slightly different continuum and CA results due to integer rounding.

To determine the length of the elongating tissue we only need consider a single row of the lattice. The length is predetermined by n. In contrast, the position of other tracked agents within the tissue [e.g., blue, green, red, light blue, and pink agents in Fig. 3(c)] is stochastic. Therefore the CA model always predicts the same rate of tissue elongation as the continuum model. However, the CA model provides additional important individual-level data regarding the detailed movements within the tissue. These individual data are stochastic and mimic the interesting nonuniformity and randomness expected in biological processes. This variability will now be analyzed.

C. Statistical analysis

For N realizations of a simulation, we define the average horizontal position of agents located initially at $p_j(x_0,y_0,0)=x_0$ as

$$\bar{p}(x_0,t) = \frac{1}{NY}\sum_{j=1}^{N}\sum_{y_0=1}^{Y} p_j(x_0,y_0,t). \quad (12)$$

It is worthwhile to note that $\bar{p}(X(0),t)=p_j(X(0),y_0,t)$, since $p_j(X(0),y_0,t)$ is independent of y_0, and represents the discrete version of $X(t)$.

The time evolution of various points in the tissue is illustrated in Fig. 3(d). The solid curves show the continuum paths for various x_0. The data points are the average positions from the $N=10$ realizations of the simulation, given by $\bar{p}(x_0,t)$. The agreement between the CA and continuum model is excellent. Qualitatively similar results are obtained for different $X(0)$ and σ_X. This is an important outcome. While the CA model was designed to exactly replicate the total length predicted by the continuum model, it is not obvious that the average CA model predictions would match the corresponding continuum results. Indeed, for a single simulation [Fig. 3(c)] the spatial distribution of the tracked

agents is nonuniform because of its inherent stochasticity. This result is analyzed further by considering the probability distribution associated with our CA rules.

From the CA data we also determine the standard deviation

$$s(x_0,t) = \sqrt{\frac{1}{NY-1}\sum_{j=1}^{N}\sum_{y_0=1}^{Y}[p_j(x_0,y_0,t)-\bar{p}(x_0,t)]^2} \quad (13)$$

and skewness

$$k(x_0,t) = \frac{1}{s(x_0,t)^3 NY}\sum_{j=1}^{N}\sum_{y_0=1}^{Y}[p_j(x_0,y_0,t)-\bar{p}(x_0,t)]^3. \quad (14)$$

At positions $x=0$ and $x=p_j(X(0),y_0,t)$ the standard deviation is zero and the skewness is infinite.

The CA statistics are related to the Pólya-Eggenberger distribution, also known as the Pólya distribution [24]. When formulated in 1923, the distribution was expressed in terms of random drawings of colored balls from an urn [24]. In terms of our variables, initially there are x_0 white balls and $X(0)-x_0$ black balls. One ball is drawn at random, and then replaced along with r balls of identical color. If this is repeated M times, and K represents the total number of times a white ball is drawn, then the distribution of K is the Pólya distribution with parameters M, x_0, $X(0)-x_0$, and r.

Here we show how our discrete model can be described in terms of a Pólya distribution. Consider a single row in the lattice of the CA model. Initially there are $X(0)$ agents in the row. Consider the position of an agent initially at x_0 where $x_0=1,\ldots,X(0)$. We track the position of this agent given by $p_j(x_0,y_0,t)$. Now K is the total number of times an agent to the left of, and including, $p_j(x_0,y_0,t)$ is chosen to proliferate. Since proliferation involves the insertion of another agent to the left of the chosen agent, as illustrated in Fig. 3(a), K is a Pólya distribution, with $r=1$.

The probability that k agents are chosen to the left of, and including, $p_j(x_0,y_0,t)$ for $M(t)=p_j(X(0),y_0,t)-X(0)$ random choices of agents is

$$\Pr(K=k,M) = \frac{\binom{M}{k}\prod_{i=0}^{k-1}(P+i\alpha)\prod_{i=0}^{M-k-1}(Q+i\alpha)}{\prod_{i=0}^{M-1}(1+i\alpha)}, \quad (15)$$

where

$$P = \frac{x_0}{X(0)}, \quad Q = 1 - \frac{x_0}{X(0)}, \quad \alpha = \frac{r}{X(0)}. \quad (16)$$

We have chosen to keep r general here. Although our interest will be for the case $r=1$, further comments on relevant parameter values will be made.

The mean, variance, and skewness are

$$\mu = MP, \quad s^2 = MPQ\frac{(1+M\alpha)}{(1+\alpha)}, \quad k = \frac{(1-2P)(1+2M\alpha)}{\sigma(1+2\alpha)}. \quad (17)$$
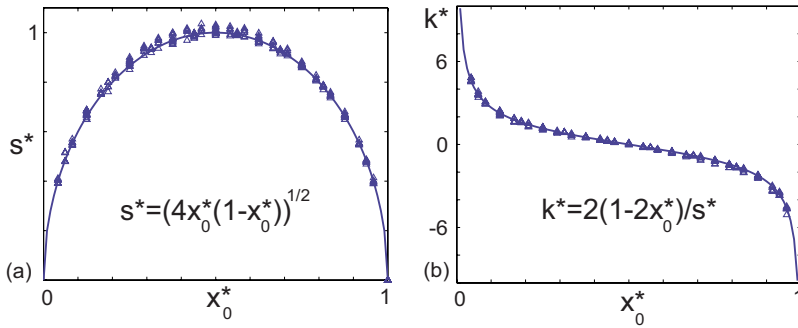
FIG. 4. (Color online) Descriptive statistics for the CA model. Data points represent results for 12 combinations of the parameters σ_X = {0.22, 0.41}, $X(0)$ = {16, 24}, and t = {1, 2, 3}. N = 200. (a) s^* versus x_0^*. (b) k^* versus x_0^*. Solid lines are the theoretical results.

To illustrate the relationship between the simulation data and Pólya distribution, we rescale the variables as

$$x_0^* = \frac{x_0}{X(0)}, \quad s^{*2} = \frac{4s^2(1+\alpha)}{M(1+M\alpha)}, \quad k^* = \frac{2ks(1+2\alpha)}{s^*(1+2M\alpha)}. \tag{18}$$

Substituting (18) into (17) gives

$$s^* = \sqrt{4x_0^*(1-x_0^*)}, \quad k^* = \frac{2(1-2x_0^*)}{s^*}. \tag{19}$$

Plots of s^* and k^* are given in Fig. 4. The statistics for the scaled CA data are illustrated for various $X(0)$, σ_X, and t. We observe that the scaled standard deviation and skewness given by the Pólya distribution (19) give an excellent fit to all the data. As the number of simulations N increases, the goodness of fit increases.

Variations in the CA mechanism can be related to different values of r. We describe some examples. (i) Integer values of $r > 1$ correspond to multiple agents being inserted into a row of the lattice. This is unrealistic for our application since each agent divides into two daughter agents only. (ii) If only the initial $X(0)$ agents are allowed to proliferate, by mitotic division, then this corresponds to $r = 0$, giving the binomial distribution. Again this is unrealistic in the biological problem under consideration, since daughter agents are also proliferative. (iii) If we change our CA proliferation mechanism to allow only the mitotic division of agents that are generated at previous time steps, then we find that the CA statistics match those of the Pólya distribution for a noninteger value of r such that $0 < r < 1$. This mechanism prevents daughter agents born within a time step from proliferating during that time step. (iv) The case $r < 0$, provided $X(0) + r(M-1) > 0$ [24], also gives a valid Pólya distribution that corresponds to agent death.

For the mitotic division of agents and $0 \leq r \leq 1$, the mean position of the tracked agents is given by

$$\bar{p}(x_0, t) = x_0 + \mu. \tag{20}$$

In Fig. 3(d), the colored markers represent these positions for our model where $r = 1$, while the solid lines represent the continuum paths given by Eq. (11).

To summarize, our CA model can be described by a Pólya distribution. In particular, the sample mean $\bar{p}(x_0, t)$ approximates paths given by the continuum model and is related to

the mean of the Pólya distribution. The scaled CA standard deviation and skewness are given by the Pólya distribution, illustrated in Fig. 4.

D. Uniform biaxial growth model

Consider now a rectangular piece of tissue that grows along both axes, where the length is $0 < x < X(t)$, and the width is $0 < y < Y(t)$. A sketch of the growth is illustrated in Fig. 5(a). If the growth is uniform, then the induced local velocity is $\mathbf{v} = u(x,t)\hat{\mathbf{x}} + v(y,t)\hat{\mathbf{y}}$, where

$$\frac{dX}{dt} = \int_0^{X(t)} \frac{\partial u}{\partial x} dx, \quad \frac{dY}{dt} = \int_0^{Y(t)} \frac{\partial v}{\partial y} dy. \tag{21}$$

For uniform growth, the growth rate is independent of position [6,25]:

$$\frac{\partial u}{\partial x} = F(t), \quad 0 < x < X(t), \quad \frac{\partial v}{\partial y} = G(t), \quad 0 < y < Y(t). \tag{22}$$

Combining Eqs. (21) and (22) gives

$$\frac{1}{X}\frac{dX}{dt} = F(t), \quad \frac{1}{Y}\frac{dY}{dt} = G(t). \tag{23}$$

Note that, without loss of generality, we have chosen $u(0,t) = v(0,t) = 0$.

The time evolution of a point (x_0, y_0) in the rectangular domain can be determined using

$$\frac{dx}{dt} = u(x,t), \quad \frac{dy}{dt} = v(y,t), \quad x(0) = x_0, \quad y(0) = y_0. \tag{24}$$

The local growth rate determines the velocity field as

$$u(x,t) = \int_0^x \frac{\partial u}{\partial \xi} d\xi, \quad v(y,t) = \int_0^y \frac{\partial v}{\partial \xi} d\xi. \tag{25}$$

For constant growth rates σ_X and σ_Y, respectively, then

$$x(t) = x_0 e^{\sigma_X t}, \quad y(t) = y_0 e^{\sigma_Y t}. \tag{26}$$

To illustrate biaxial growth, a growth rate in each direction must be specified. Instead of using a constant growth rate, as done in Sec. II A, we present results for logistic growth in the x direction and linear growth in the y direction. We choose the length and width of the tissue to evolve as

FIG. 6. (Color online) Trajectories from the continuum model of selected initial positions on a biaxially growing tissue with $X(0) = Y(0) = 10$. Growth in the x direction is logistic with $\alpha = 0.70$ and $K = 20$, while growth in the y direction is linear with $\beta = 1$. Green markers represent the selected initial positions (x_0, y_0). The red markers are the evolved positions (x, y) at $t = 10$ of the green markers.

$$x(t) = x_0 \frac{K}{X(0) + [K - X(0)]e^{-\alpha t}}, \quad y(t) = y_0 \left(1 + \frac{\beta t}{Y(0)}\right),$$

$$(29)$$

respectively. Equation (29) gives the continuum paths for uniform biaxial growth.

We extend the CA model to include biaxial growth. The mechanism that increases the width of the lattice is similar to the rule for uniaxial growth [Fig. 3(a)]. For a single time step of the CA algorithm, n agents in each row and m agents in each column are chosen to proliferate. There are a number of ways to choose the order in which the new agents are inserted into either the rows or columns. For example, the row insertions can all be made first followed by the column insertions, or vice versa. Another way is to alternate between each of the row and column insertions. These three methods (and others) gave similar results.

For biaxial growth we track agents in both dimensions. Let $p_j(x_0, y_0, t)$ and $q_j(x_0, y_0, t)$ be the horizontal and vertical positions of an agent initially at position (x_0, y_0), so that $p_j(x_0, y_0, 0) = x_0$ and $q_j(x_0, y_0, 0) = y_0$. Analogous to the definition of $\bar{p}(x_0, t)$ in Eq. (12), we define the average vertical position of an agent over N realizations of a simulation as

$$\bar{q}(y_0, t) = \frac{1}{NX(0)} \sum_{j=1}^{N} \sum_{x_0=1}^{X(0)} q_j(x_0, y_0, t). \quad (30)$$

Similarly to uniaxial growth, $\bar{q}(Y(0), t) = q_j(x_0, Y(0), t)$, since $q_j(x_0, Y(0), t)$ is independent of x_0, and represents the discrete version of $Y(t)$. The standard deviation and skewness of
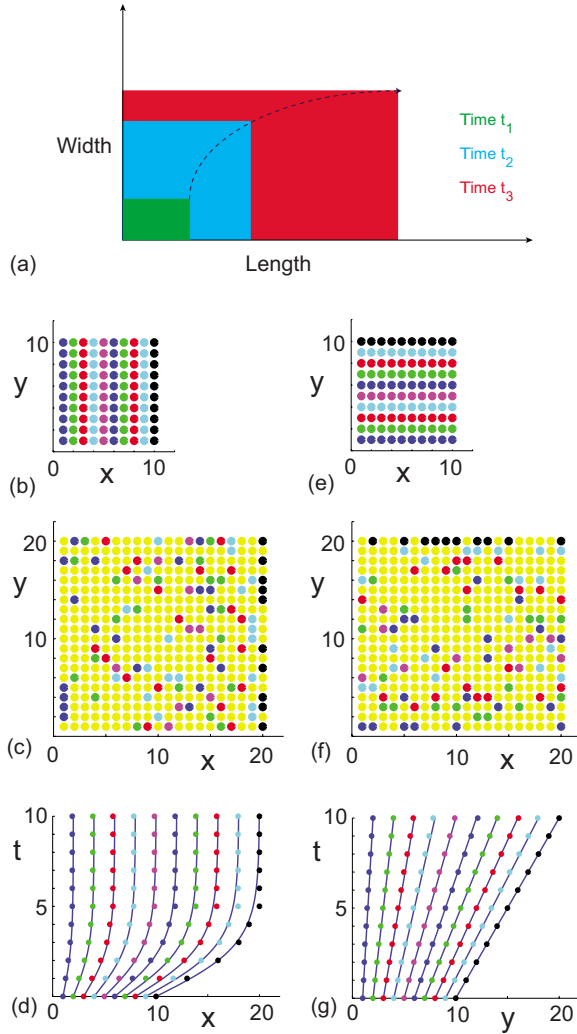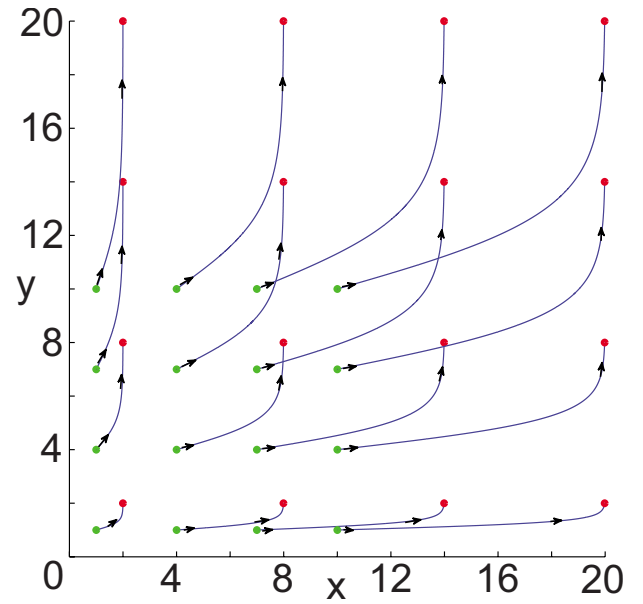

FIG. 5. (Color online) Biaxial tissue growth. (a) Schematic of biaxial growth. (b)–(g) Growth in the x direction is logistic with $\alpha = 0.70$ and $K = 20$, while growth in the y direction is linear with $\beta = 1$, $X(0) = Y(0) = 10$. (b) Columns of agents to be tracked in the x direction. (c) Positions of tracked agents marked in (b) at $t = 10$. (d) Space-time diagram of the paths (solid curves) from the continuum model and the average values (markers) $\bar{p}(x_0, t)$ from $N = 25$ simulations of the CA model. (e) Rows of agents to be tracked in the y direction. (f) Positions of tracked agents marked in (e) at $t = 10$. (g) Space-time diagram of the paths (solid curves) from the continuum model and the average values (markers) $\bar{q}(y_0, t)$ from $N = 25$ simulations of the CA model.

$$X(t) = \frac{X(0)K}{X(0) + [K - X(0)]e^{-\alpha t}}, \quad Y(t) = Y(0) + \beta t, \quad (27)$$

with the corresponding growth rates, Eq. (23), given by

$$F(t) = \alpha \left(1 - \frac{X(t)}{K}\right), \quad G(t) = \frac{\beta}{Y(t)}. \quad (28)$$

The time evolution of the coordinates of a trajectory starting at (x_0, y_0) within the tissue is given by
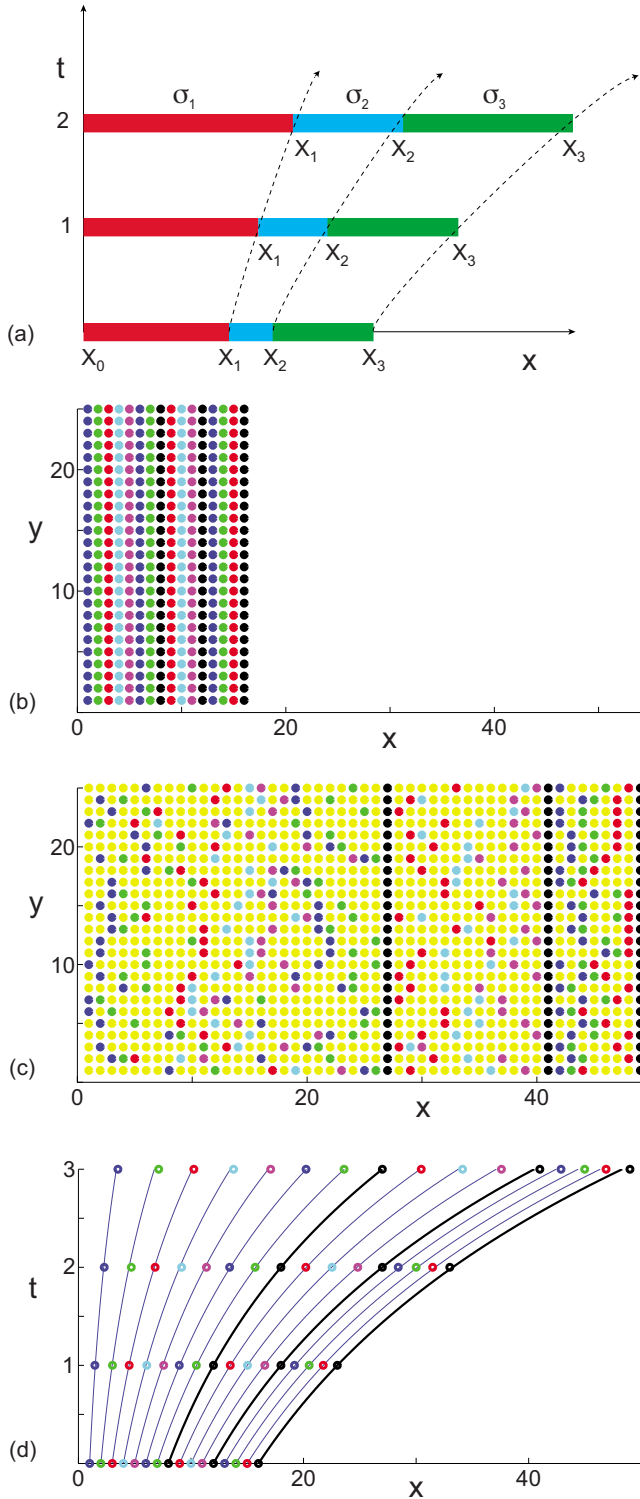
FIG. 7. (Color online) Nonuniform uniaxial growth. (a) Schematic space-time diagram of the continuum growth model with $M = 3$. In (b)-(d) the values of the parameters for the initial positions of the biological landmarks and the growth rates are $X_1(0)=8$, $X_2(0) =12$, $X_3(0)=16$, $\sigma_1=\sigma_2=0.41$, and $\sigma_3=0.22$. (b) Columns of agents of the same color at $t=0$ to be tracked for $t>0$, $Y=25$. The black columns represent the landmarks. (c) Positions of tracked agents at $t=3$. (d) Space-time diagram of the paths (solid curves) from the continuum model and the average values (markers) $\bar{p}(x_0,t)$ from $N=10$ simulations of the CA model.

the CA data for agents being tracked in the y direction are calculated using equations analogous to Eqs. (13) and (14).

Results for the biaxial growth are given in Fig. 5 and 6. As for the previous uniaxial results, the length, width, and average horizontal and vertical positions, $\bar{p}(x_0,t)$ and $\bar{q}(y_0,t)$, within the growing tissue predicted by the CA model, coincide with the continuum results (Fig. 5). The trajectories from the continuum model in the Cartesian plane are shown in Fig. 6 for a selection of initial positions (x_0,y_0) on a biaxially growing tissue. The trajectories in Fig. 6 are for the same values of the parameters as the space-time diagrams of Fig. 5.

We further analyzed the statistics of the CA data for biaxial growth. Because of the independence of the growth along each axis, the scaled standard deviation and skewness for both dimensions also collapse onto the curves in Fig. 4.

III. NONUNIFORM UNIAXIAL GROWTH MODEL

In certain applications, the assumption of uniform uniaxial growth may be invalid. The continuum and CA models can be adapted to model nonuniform uniaxial growth by representing the tissue as a series of piecewise uniformly growing subsections. Suppose X_i, for $i=0,1,\ldots,M$, are the positions of $M+1$ landmarks along a growing tissue. Observational data can describe the evolution of these positions with time t, so that $X_i(t)$ is given at discrete times. Without loss of generality, we choose $X_0(t)=0$ for all time. The total length of the tissue is $X_M(t)$. A schematic diagram of nonuniform uniaxial growth is shown in Fig. 7(a) with different constant growth rates σ_i, for $i=1,\ldots,M$, in each subsection.

If tissue growth between adjacent landmarks X_i and X_{i-1} is uniform with constant growth rate σ_i, then

$$\frac{\partial u}{\partial x} = \sigma_i, \quad X_{i-1}(t) < x < X_i(t), \tag{31}$$

and

$$\frac{1}{X_i - X_{i-1}}\frac{d}{dt}(X_i - X_{i-1}) = \sigma_i. \tag{32}$$

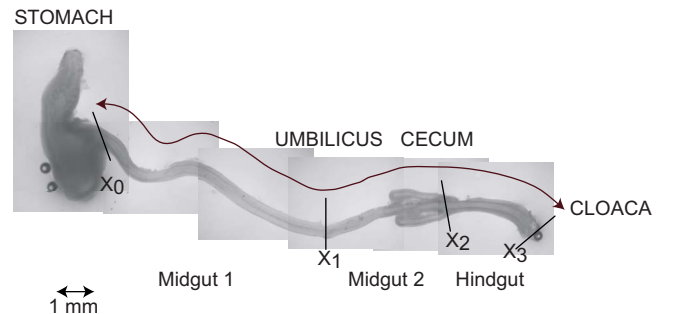Hence, each subsection of tissue grows exponentially as

FIG. 8. (Color online) Image of an E6 quail embryo illustrating the landmarks along the gut and nomenclature used to describe the growth dynamics.
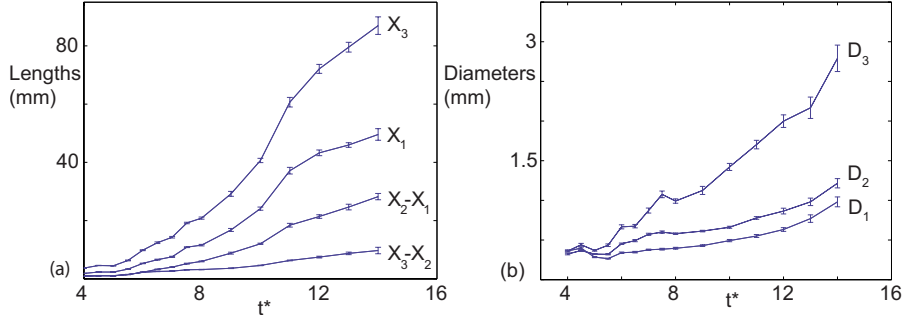
FIG. 9. (Color online) Measurements of the gut for age E4 to E14. The error bars are for the standard error $s/\sqrt{n}$. (a) Arclength of gut sections and total arclength. (b) Diameter of the gut measured at the landmarks.

$$X_i(t) - X_{i-1}(t) = [X_i(0) - X_{i-1}(0)]e^{\sigma_i t}. \quad (33)$$

The position of each landmark in a series of uniformly growing subsections of tissue is given by

$$X_i(t) = \sum_{j=1}^{i} [X_j(0) - X_{j-1}(0)]e^{\sigma_j t}. \quad (34)$$

Now the local growth rate determines the velocity field as

$$u(x,t) = \int_0^x \frac{\partial u}{\partial \xi} d\xi = \sigma_i[x - X_i(t)] + \sum_{j=1}^{i} \sigma_j[X_j(t) - X_{j-1}(t)],$$
$$(35)$$

for $X_{i-1}(t) < x < X_i(t)$. Combining Eqs. (9) and (35) gives the evolving path of a point initially at x_0 as

$$x(t) = [x_0 - X_i(0)]e^{\sigma_i t} + \sum_{j=1}^{i} [X_j(0) - X_{j-1}(0)]e^{\sigma_j t}, \quad (36)$$

for $X_{i-1}(t) < x < X_i(t)$. In summary, we have described how to model a nonuniformly growing tissue using a series of piecewise uniform subsections of tissue [18]. In the case that all the growth rates σ_i are equal, then the model relaxes to a uniform uniaxial growth model.

For the jth realization of the CA model, the length of the lattice is increased at different rates in the subsections $p_j(X_{i-1}(0), y_0, t) < x < p_j(X_i(0), y_0, t)$ for $i = 1, \ldots, M$. Each landmark must remain at the same position in each row of the lattice. Equation (33) shows that the increase in the length $X_i(t) - X_{i-1}(t)$ from time t to $t+1$ in the continuum model is $[X_i(t) - X_{i-1}(t)](e^{\sigma_i} - 1)$. Therefore, we define n as the nearest integer value or 'round' of $[(p_j(X_i(0), y_0, t) - p_j(X_{i-1}(0), y_0, t)](e^{\sigma_i} - 1)$. In each time step of the CA model, n agents in each row proliferate at random positions between the two landmarks and n new agents are inserted, as described in Fig. 3(a). When a new agent is inserted, the position of the right-hand landmark is updated. The positions of the two landmarks at the beginning of the time step are $p_j(X_{i-1}(0), y_0, t)$ and $p_j(X_i(0), y_0, t)$, and the positions of the two landmarks at the end of the time step are $p_j(X_{i-1}(0), y_0, t+1)$ and $p_j(X_i(0), y_0, t+1) = p_j(X_{i-1}(0), y_0, t+1) - p_j(X_{i-1}(0), y_0, t) + p_j(X_i(0), y_0, t) + n$.

Figure 7(c) shows a typical CA simulation with three subsections for the initial condition in Fig. 7(b). The average position of the tracked agents agree with the continuum paths in Fig. 7(d). Scaled CA data of the standard deviation and skewness for each subsection also collapse onto the curves in Fig. 4.

The nonuniformity in the continuum model and average horizontal position of the tracked agents in the CA model are shown in Fig. 7(d). Because of the lower growth rate in the third subsection, the spacings between the paths in that subsection are narrower than in the first two subsections. In Sec. IV we demonstrate that it is necessary to use a nonuniform uniaxial growth model to accurately predict the position of landmarks along the developing quail gut.

IV. CASE STUDY: NONUNIFORM GUT LENGTH ELONGATION

The continuum and CA uniaxial growth models will now be applied to elongation data for the developing intestinal tract of a quail embryo.

A. Observational data

The morphology of a developing quail gut is shown in Fig. 8. Four biological landmarks are identified along the gut, namely, (i) the stomach, (ii) the umbilicus, (iii) the cecum, and (iv) the cloaca. The landmarks are denoted X_i, where the stomach is fixed at $X_0(t) = 0$ and the cloaca is $X_3(t)$. The subsections between these landmarks are called midgut 1, midgut 2, and hindgut, respectively [7]. The arclength and diameter of each subsection were measured between embryonic age 4 days (E4) and E14 and are shown in Fig. 9. The growth of each subsection of tissue shows similar trends.

First we consider the elongation of the tissue. From E4 to E11, the length of each subsection increases exponentially

TABLE I. Elongation and thickening growth rates in the gut.

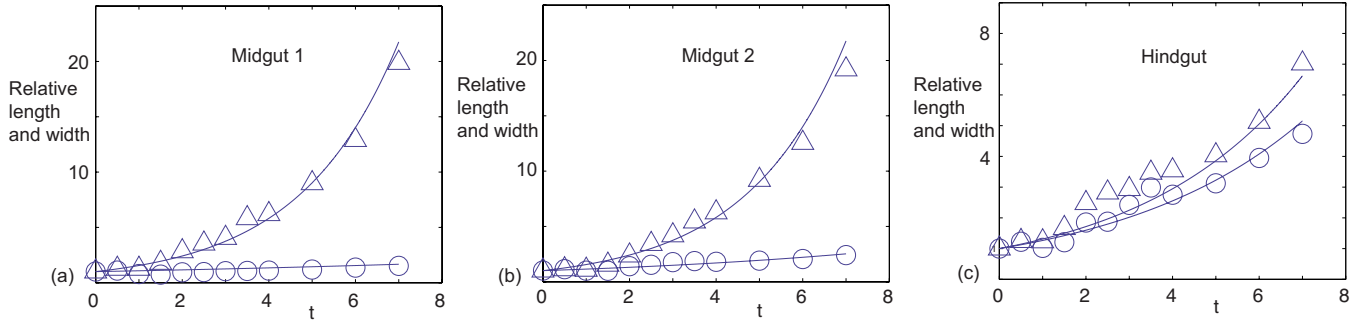| Growth rates	Midgut 1	Midgut 2	Hindgut
σ_X	0.44	0.44	0.27
σ_Y	0.08	0.13	0.23
$\sigma = \sigma_X + \sigma_Y$	0.52	0.57	0.50

FIG. 10. (Color online) Relative lengths L_i (triangles) and widths W_i (circles) for the three gut subsections with $t=t^*-4$. (a) Midgut 1: $\sigma_X=0.44$, $\sigma_Y=0.08$. (b) Midgut 2: $\sigma_X=0.44$, $\sigma_Y=0.13$. (c) Hindgut: $\sigma_X=0.27$, $\sigma_Y=0.23$.

and at later times the rate of increase slows so that the growth profile resembles part of a logistic curve. The growth data are of interest because it is an important mechanism that influences NC cell migration during development of the ENS. During normal development NC cells colonize the entire gut by E8 [26]. Therefore, we need only focus upon the exponential part up to this age. However, since the exponential growth lasts up to E11, we will model the exponential gut growth over this period of seven days.

There is some radial expansion of the gut as seen in Fig. 9(b). The diameters can also be described by an exponential growth model.

To assess any spatial variability in the growth rates, we evaluate the relative elongation and radial expansion in each subsection. Again considering each cylindrical shell as a rectangle with a fixed thickness, we can describe the relative lengths L_i and relative widths W_i as

$$L_i = \frac{X_i(t) - X_{i-1}(t)}{X_i(0) - X_{i-1}(0)} \quad \text{and} \quad W_i = \frac{D_i(t)}{D_i(0)} \quad (37)$$

of the ith subsection. This data is illustrated in Fig. 10. The increase in the relative length of the subsections with time shows that there is very little difference in the elongation of midgut 1 and midgut 2, whereas the hindgut elongates at a reduced rate. Different rates of elongation in the three subsections give an excellent fit to the data [Figs. 10(a) and 10(b)] and imply that the overall growth rate is nonuniform along the gut tissue.

The relative elongation in length and radial expansion are different in the different regions of the gut. For example, in midgut 1 and midgut 2, the radial growth is negligible com-

pared to the elongation. However, in the hindgut the two growth rates are similar and therefore the growth is nearly isotropic.

In summary, each subsection of tissue grows exponentially in length X and width Y while the thickness Z of the tissue remains constant. For each subsection, growth rates σ_X and σ_Y can be determined (with $\sigma_Z=0$). Arguments outlined in Sec. I indicate that the sum of these growth rates ought to be a constant in all subsections of the tissue. Data in Table I shows that the total growth rate $\sigma=\sigma_X+\sigma_Y$ is approximately constant in all subsections. This is consistent with the assumption that the cell numbers are increasing exponentially in number, giving rise to an exponentially growing volume. However, here, for example, the midgut regions are growing anisotropically, whereas the growth is almost isotropic in the hindgut. These data support the arguments outlined in Sec. I and provide a potential explanation of how midgut 1 and midgut 2 elongate much more than the hindgut, even though these subsections are composed of the same cells which presumably proliferate at the same rate. The mismatch is explained by the hindgut radially expanding far more than midgut 1 and midgut 2.

Tables II and III in the Appendix give details of the arclength and diameter measurements. For completeness we also include a short analysis of data describing the increase in the length of the cecum or cecal lobe [Fig. 11(a)]. Measurements were made from E5.5, as prior to this time the length of the cecal lobe is too small to measure. Its relative length [Fig. 11(b)] was found to grow exponentially versus $t=t^*-5.5$.

B. Comparison of models and observational data

For simplicity, we focus on gut elongation. This is more important since NC cells must invade down the whole ex-

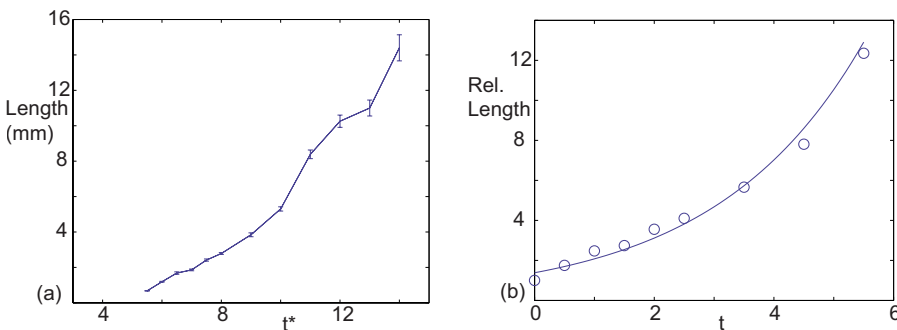

FIG. 11. (Color online) Cecal lobe growth data from Table III. (a) Arclength. The error bars are for the standard error $s/\sqrt{n}$. (b) Relative length (circles). The solid curve is for an exponential growth model, growth rate $\sigma_C=0.41$.
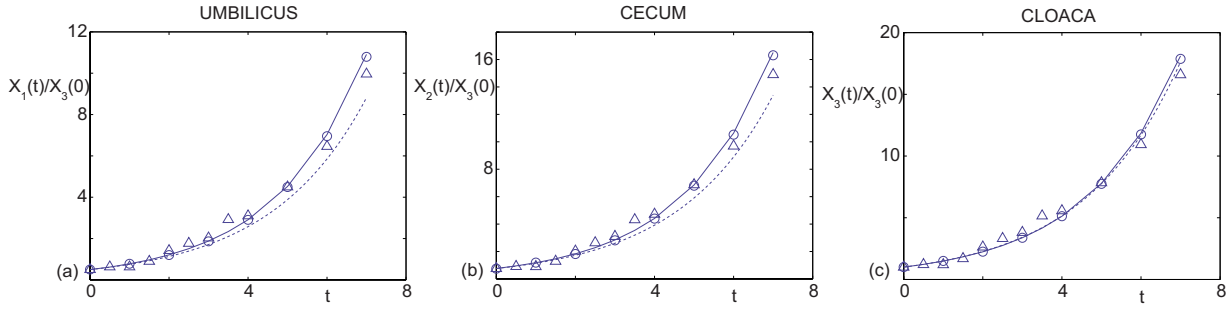
FIG. 12. (Color online) Scaled data from Table II (triangles). (a) Umbilicus. (b) Cecum. (c) Cloaca. Nonuniform CA model (circles), nonuniform continuum model (solid curves), and uniform continuum model (broken curves). Initial values for the landmarks and growth rates used in the models are $X_1(0)/X_3(0)=0.50$, $X_2(0)/X_3(0)=0.76$, $X_3(0)/X_3(0)=1.00$, $\sigma_1=0.44$, $\sigma_2=0.44$, $\sigma_3=0.27$, and $\sigma_L=0.41$.

panding length of the gut to ensure normal development [26].

To assess the effectiveness of the continuum and CA models at predicting the positions of the biological landmarks, the observational data are rescaled. From the original data the rescaled positions $X_i(t)/X_3(0)$ of the landmarks, at time $t=t^*-4$, are given in Fig. 12.

Using the estimates for the growth rates $\sigma_1=\sigma_2=0.44$ and $\sigma_3=0.27$ in the three subsections [Figs. 10(a)–10(c)], Eq. (34) gives the evolution in time of the landmarks for the continuum model. Appropriately chosen integer values for the initial positions of the landmarks and growth rates were used to match the position of the landmarks with the CA model. Figure 12 shows that the continuum and CA results are indistinguishable and compare well with the observational data, as expected.
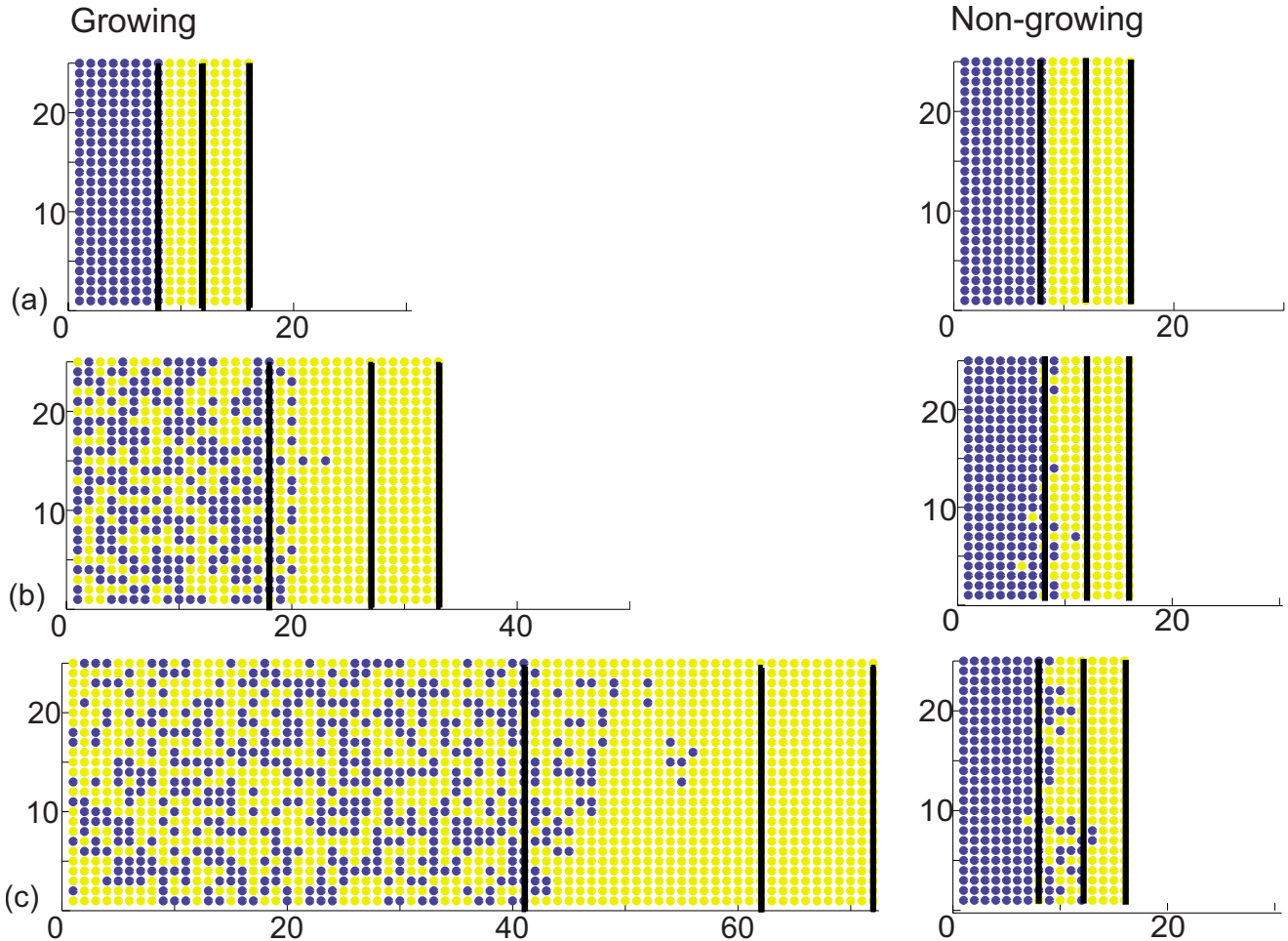

FIG. 13. (Color online) NC cell invasion on a growing ($\sigma_1=\sigma_2=0.41$, $\sigma_3=0.22$) and a nongrowing tissue, $X_1(0)=8$, $X_2(0)=12$, and $X_3(0)=16$. (a) Number $n=200$ of NC agents (blue) at $t=0$. (b) Growing tissue ($n=272$) and nongrowing tissue ($n=203$) at $t=2$. (c) Growing tissue ($n=501$) and nongrowing tissue ($n=227$) at $t=4$.

We emphasize the importance of using a nonuniform elongation model. Results from a uniform growth elongation model with a single constant growth rate $\sigma_L = 0.41$ for the entire length of gut are compared with the nonuniform model and observational data (Fig. 12). The uniform uniaxial model accurately predicts the position of the cloaca, but underestimates the positions of the umbilicus and the cecum [Figs. 12(a) and 12(b)]. Therefore the nonuniform elongation model is necessary to simulate the dynamics of the landmark positions.

V. DISCUSSION AND CONCLUSIONS

We have developed a discrete and a continuous model to describe tissue growth. The models can be applied to represent uniaxial tissue elongation or biaxial expansion. Both models have the flexibility to be applied to a single region of tissue undergoing uniform growth, or to represent a nonuniformly elongating tissue as a series of piecewise uniform subsections of tissue.

The discrete model is designed so that the increase in length and width of each subsection is equivalent to the continuum model. Our simulations and analysis show that the average position of any point within the tissue predicted by the CA algorithm coincides with the continuum model. This is a unique feature since the discrete model predicts the same average properties as the continuum model while also providing additional insight into growth process at a level that is unresolved by the continuum model. The individual-level behavior and stochasticity of the CA model reflect real biological behaviors.

Our CA tissue growth model provides an additional application for the Pólya distribution. The distribution also appears in models of nuclear fragmentation and clustering, genetic diversity, the social behavior of monkeys, and the group behavior of people [27–29].

Using observational data for the development of the avian gut, we showed that a nonuniform model is required to predict the location of measurable landmarks. While the observational data indicated that the increase in length and width of the developing gut were nonuniform, the increase in length was much more pronounced than the increase in width along most sections of the developing tissue. Therefore we chose to represent the developing gut as a series of three elongating sections of tissue and ignored the increase in diameter.

The CA model provides a framework for modeling a growing tissue coupled with other biological mechanisms. One such system is the NC cell invasion along the developing gut [30,31]. Typically NC cells invade the thick intestinal mesenchymal cell mass, but are restricted to a narrow layer, as on the surface of a cylinder. This two-dimensional format is particularly amenable to our CA model. Simulations of NC cell invasion on an elongating tissue are presented in Fig. 13 and are compared to an equivalent simulation on a nongrowing tissue. Neighbor-excluded motility and proliferation mechanisms for the NC agents similar to those described by Simpson *et al.* [32] are used to represent NC cell behavior. Identical NC motility and proliferation rates were used in the growing and nongrowing tissue simulations.
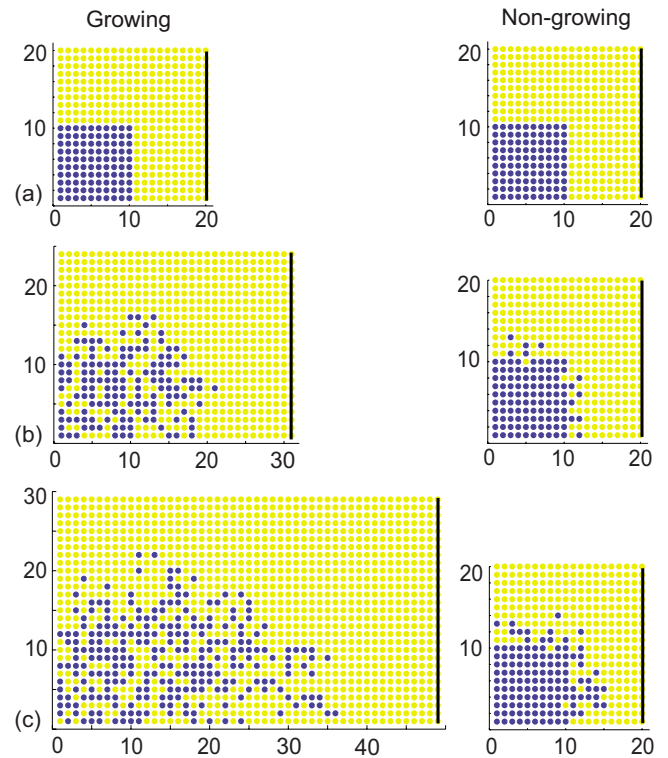

FIG. 14. (Color online) NC cell invasion on a growing ($\sigma_X = 0.22$, $\sigma_Y = 0.10$) and a nongrowing tissue, $X(0) = Y(0) = 20$. (a) Number $n = 100$ of NC agents (blue) at $t = 0$. (b) Growing tissue ($n = 139$) and nongrowing tissue ($n = 110$) at $t = 2$. (c) Growing tissue ($n = 254$) and nongrowing tissue ($n = 130$) at $t = 4$.

Several observations can be made from the simulations in Fig. 13. At the later times shown, there is a larger number of NC agents on the growing tissue than the nongrowing tissue. This arises because the expanding tissue provides extra space for NC agent proliferation. Moreover, the NC cell invasion along the gut toward the anal (cloaca) end is more advanced, relative to the position of the cloaca on the nongrowing tissue.

To further generalize these observations, simulations of motility and proliferation on a biaxially growing tissue, with anisotropic exponential growth in both the length and width, are given in Fig. 14. Similarly to the uniaxial results, there are more cells on the growing tissue than an the nongrowing tissue at later times, and the distance along the growing tissue relative to the length and width of the tissue is more advanced in the nongrowing case.

In summary, these simulations illustrate complex interactions between NC cell motility and proliferation and the growth of the underlying tissue. These interactions determine, in part, the ability of the NC cell population to colonize the growing gut tissues.

Our approach is not limited to developmental biology applications. This work provides a useful and promising framework for studying complex interactions between growing domains in general and the transport and reaction of materials on that domain, for example in material swelling associated with solute migration [33,34].

TABLE II. Average lengths of the gut taken at time t^* (days). Measurements in mm, variance s^2, and sample size n.

t^*	n	X_3	s^2	X_1	s^2	X_2-X_1	s^2	X_3-X_2	s^2
4.0	19	3.7	0.06	1.9	0.03	0.96	0.01	0.90	0.01
4.5	14	4.6	0.05	2.3	0.03	1.07	0.01	1.12	0.02
5.0	28	4.5	0.13	2.3	0.05	1.03	0.04	1.11	0.01
5.5	12	6.3	0.26	3.3	0.08	1.47	0.03	1.50	0.01
6.0	21	9.8	0.56	5.3	0.23	2.27	0.05	2.23	0.03
6.5	13	12.4	1.02	6.6	0.41	3.27	0.19	2.54	0.06
7.0	15	14.3	1.09	7.6	0.61	4.02	0.15	2.64	0.10
7.5	14	19.2	0.90	10.9	0.28	5.22	0.42	3.12	0.06
8.0	17	20.9	2.33	11.6	1.14	6.01	0.41	3.19	0.10
9.0	14	29.2	9.98	16.8	3.62	8.83	1.44	3.63	0.12
10.0	15	40.7	7.96	24.1	4.43	12.04	0.75	4.61	0.14
11.0	15	60.7	40.54	37.1	19.34	18.42	6.01	6.32	0.30
12.0	8	72.1	18.80	43.3	7.61	21.40	3.02	7.47	0.75
13.0	8	79.6	22.46	45.0	5.02	24.65	7.60	8.75	1.53
14.0	8	86.0	72.80	49.6	31.63	28.24	9.22	9.73	9.85

APPENDIX: OBSERVATIONAL DATA

Tables II and III give the observational data for the length and width data, respectively. Table II gives the lengths of the three subsections and total length of the gut. Table III gives the diameter D_i of the gut at three of the landmarks and the length of the cecal lobe C.

TABLE III. Average diameter D_i at three of the landmarks and length of the cecal lobe C taken at time t^* (days). Measurements in mm, variance s^2, and sample size n.

t^*	n	D_3	s^2	D_2	s^2	D_1	s^2	C	s^2
4.0	21	0.36	0.002	0.32	0.000	0.36	0.004		
4.5	14	0.44	0.004	0.37	0.001	0.40	0.003		
5.0	28	0.37	0.002	0.32	0.001	0.28	0.001		
5.5	12	0.43	0.003	0.32	0.001	0.27	0.001	0.68	0.004
6.0	21	0.67	0.014	0.45	0.002	0.34	0.002	1.19	0.013
6.5	13	0.67	0.006	0.49	0.003	0.35	0.001	1.68	0.060
7.0	15	0.87	0.015	0.57	0.003	0.38	0.001	1.86	0.037
7.5	14	1.08	0.025	0.60	0.003	0.38	0.002	2.42	0.055
8.0	17	0.99	0.013	0.58	0.002	0.40	0.002	2.79	0.048
9.0	14	1.13	0.036	0.61	0.001	0.43	0.002	3.84	0.168
10.0	15	1.42	0.030	0.66	0.002	0.49	0.003	5.30	0.217
11.0	15	1.70	0.043	0.78	0.004	0.55	0.005	8.39	0.887
12.0	8	2.00	0.050	0.87	0.011	0.63	0.004	10.26	0.959
13.0	8	2.17	0.146	0.98	0.018	0.77	0.018	11.00	0.617
14.0	8	2.79	0.222	1.22	0.027	0.98	0.031	14.40	4.334

[1] R. Keller, Science **298**, 1950 (2002).

[2] R. Keller, Development **133**, 2291 (2006).

[3] D. C. Myers, D. S. Sepich, and L. Solnica-Krezel, Trends Genet. **18**, 447 (2002).

[4] L. Wolpert, *Principles of Development* (Oxford University Press, Oxford, 2002).

[5] N. M. Le Douarin, Bull. Biol. Fr. Belg. **98**, 544 (1964).

[6] K. A. Landman, G. J. Pettet, and D. F. Newgreen, Bull. Math. Biol. **65**, 235 (2003).

[7] D. F. Newgreen, B. Southwell, L. Hartley, and I. J. Allan, Acta Anat. (Basel) **157**, 105 (1996).

[8] M. J. Simpson, K. A. Landman, and D. F. Newgreen, J. Comput. Appl. Math. **192**, 282 (2006).

[9] M. J. Geske, X. Zhang, K. K. Patel, D. M. Ornitz, and T. S. Stappenbeck, Development **135**, 2959 (2008).

[10] H. Meinhardt, *Models of Biological Pattern Formation* (Academic Press, London, 1982).

[11] A. M. Turing, Philos. Trans. R. Soc. London, Ser. B **237**, 37 (1952).

[12] R. Dillon and H. G. Othmer, J. Theor. Biol. **197**, 295 (1999).

[13] S. A. Newman and H. L. Frisch, Science **205**, 662 (1979).

[14] S. Kondo and R. Asai, Nature (London) **376**, 765 (1995).

[15] P. M. Kulesa, G. C. Cruywagen, S. R. Lubkin, P. K. Maini, J. Sneyd, M. W. J. Ferguson, and J. D. Murray, J. Theor. Biol. **180**, 287 (1996).

[16] E. J. Crampin, E. A. Gaffney, and P. K. Maini, Bull. Math. Biol. **61**, 1093 (1999).

[17] E. J. Crampin and P. K. Maini, Comments Theor. Biol. **6**, 229 (2001).

[18] E. J. Crampin, W. W. Hackborn, and P. K. Maini, Bull. Math. Biol. **64**, 747 (2002).

[19] K. J. Painter, Ph.D. thesis, University of Oxford, 1997.

[20] R. E. Baker and P. K. Maini, J. Math. Biol. **54**, 597 (2007).

[21] S. M. Peirce, T. C. Skalak, and J. A. Papin, IBM J. Res. Dev. **50**, 601 (2006).

[22] B. C. Thorne, A. M. Bailey, D. W. DeSimone, and S. M. Peirce, Birth Defects Res. C **81**, 344 (2007).

[23] S. Turner, J. A. Sherratt, K. J. Painter, and N. J. Savill, Phys. Rev. E **69**, 021910 (2004).

[24] N. L. Johnson, A. W. Kemp, and S. Kotz, *Univariate Discrete Distributions*, 3rd ed. (Wiley, New York, 2005).

[25] E. J. Crampin, Ph.D. thesis, University of Oxford, 2000.

[26] K. A. Landman, M. J. Simpson, and D. F. Newgreen, Dev., Growth Differ. **49**, 277 (2007).

[27] A. Z. Mekjian and S. J. Lee, Phys. Rev. A **44**, 6294 (1991).

[28] A. Z. Mekjian, Phys. Rev. A **44**, 8361 (1991).

[29] S. J. Lee and A. Z. Mekjian, Phys. Rev. C **47**, 2266 (1993).

[30] M. J. Simpson, K. A. Landman, B. D. Hughes, and D. F. Newgreen, J. Theor. Biol. **243**, 343 (2006).

[31] M. J. Simpson, D. C. Zhang, M. Mariani, K. A. Landman, and D. F. Newgreen, Dev. Biol. **302**, 553 (2007).

[32] M. J. Simpson, A. Merrifield, K. A. Landman, and B. D. Hughes, Phys. Rev. E **76**, 021918 (2007).

[33] U. Goerke, A. H. L. Chamberlain, E. A. Crilly, and P. J. McDonald, Phys. Rev. E **62**, 5353 (2000).

[34] B. R. Simon, J. P. Liable, D. Pflaster, Y. Yuan, and M. H. Krag, J. Biomech. Eng. **118**, 1 (1996).